Article

Elastic Behavior of Transversely Isotropic Cylindrical Rock Samples under Uniaxial Compression Considering Ideal and Frictional Boundary Conditions

Manuel Bernhard Winkler *⬥, Thomas Frühwirt ⬥ and Thomas Marcher ⬥

Institute of Rock Mechanics and Tunnelling, Graz University of Technology, 8010 Graz, Austria; fruehwirt@tugraz.at (T.F.)
* Correspondence: winkler@tugraz.at

Abstract: Conceptualizing sophisticated measurement set-ups as well as testing and evaluation procedures for laboratory experiments on anisotropic rocks requires a basic understanding of the potential specimen behavior. The focus of the present work was therefore to investigate the influence of different transversely isotropic parameters and their ratios on the elastic behavior of cylindrical rock samples in uniaxial compression tests. Parameter sets corresponding to soft anisotropic rocks were chosen based on naturally observed ranges for the five elastic transversely isotropic constants. Analytical results for the radial and vertical strain distributions around the sample circumference and a comparison with finite element simulations are presented. Further, the effect of interface friction between samples and loading platens was analyzed within the numerical models. The results suggest that radial strains around cylindrical anisotropic samples are rarely uniform except for specific combinations of parameters and isotropy plane inclinations. The effect of interface friction was found to have a clear influence on the developing elastic stress and strain distributions for samples with inclined isotropy planes. Nevertheless, no significant influence of frictional boundary conditions on the back-calibrated values of the elastic parameters could be identified, suggesting that friction-reducing measures in uniaxial compression tests on transversely isotropic samples with predominantly linear behavior are not required.

Keywords: transversely isotropic rock; uniaxial compression; anisotropic deformation; elastic constants; Poisson's ratio; Young's modulus

1. Introduction

Due to the formation history of rocks, they are usually associated with an anisotropic mechanical behavior. Pure isotropy is only encountered to a limited extent in natural rock formations [1], which is why the consideration of direction-dependent physical properties is all the more important in order to make realistic engineering predictions for the given task.

Anisotropy is encountered at various scales in rock engineering, from the scale of the entire rock mass down to the scale of the intact rock [2]. Intact rock anisotropy, also referred to as inherent anisotropy [3], is associated with the formation history of most sedimentary and metamorphic rocks resulting in preferential planes of cleavage, lamination, bedding, foliation or schistosity [4,5].

Paying attention to inherently anisotropic rock behavior is particularly relevant in petroleum and geothermal engineering for the assessment of the material's fracability and the prediction of wellbore stability along with deformations and stresses around boreholes [6]. Inherent elastic anisotropy is also an important factor to be considered for the interpretation of stress measurements, e.g., overcoring experiments [7,8], and other in situ tests in underground engineering, such as pressuremeter tests [9]. Consequently, a thorough determination of the intact rock's anisotropic character with respect to its physical

properties is vital. This especially holds for the evaluation of the material's orientation-dependent deformability.

Commonly, a transversely isotropic material model is adopted for the description of the elastic deformability of laminated or foliated rocks with clear visibility of the plane orientations (class B rocks) [10]. Thereby, a plane of isotropy is assumed to be present in the direction of the rocks' planar fabrics with an axis of symmetry normal to them. Five independent parameters are required to fully describe a transversely isotropic solid [11]: E and E', describing the Young's moduli parallel and normal to the plane of isotropy; the Poisson's ratios ν and ν', characterizing lateral strain in the plane of isotropy resulting from a normal strain applied within this plane and normal to it; and the transverse shear modulus G' associated with the shear modulus normal to the plane of isotropy. The shear modulus G within the isotropy plane is not an independent parameter, for which the relationship of $G = E/[2(1 + \nu)]$ is given.

The determination of the elastic constants is based on the conduction of various static and dynamic laboratory tests. For most applications in geomechanics, however, the static constants, resulting from the corresponding testing methods, are more suitable [12]. The standard procedure for the determination of the static constants represents the conduction of at least three uniaxial compressive strength (UCS) tests in directions normal, parallel and inclined to the planes of isotropy combined with oriented lateral strain measurements [10]. Cho et al. [13] suggested the use of a least-squares approximation scheme in case more than the required minimum number of strain measurements are included in the assessment of the five elastic constants. Alejano et al. [14] established a procedure for the consideration of a large number of tests for the evaluation of the elastic constants of a transversely isotropic slate relying on the solution of a non-linear optimization problem. Lately, Winkler et al. [15] developed an evaluation technique for the five elastic constants based on averaged circumferential strain measurements on cylindrical specimens in UCS tests. This was performed to increase test practicality and to reduce the influence of errors due to deviations in otherwise required oriented strain measurements from the ideal measuring directions. Improvements to the standard testing scheme, associated with the conduction of multiple tests, have been made over time, mainly to reduce the required number of tests and thus the influence of sample heterogeneity, or to account for the material's stress-dependency. Nejati et al. [16] and Shen and Playter [12] list some of the most important developments in this regard and discuss the associated benefits and deficiencies. Yim et al. [17] proposed an iterative procedure to determine the five elastic constants by conducting uniaxial compression and Brazilian tests using specimens from a single-orientation core. More recently, strip load tests on single cylindrical test specimens with arbitrary isotropy plane inclinations have been used to determine the full set of transversely isotropic constants without the need to assume approximate relationships between individual parameters or to use special test apparatuses [18,19]. While the strip load test method thus overcomes the limitations of previous methods for determining the transversely isotropic constants on single-core samples, its practicality may still be limited by the computationally expensive strain inversion method involved [18] or the lack of availability of a trained artificial neural network (ANN) [19]. Despite ongoing developments with regard to calibration methods to derive transversely isotropic constants from tests on single samples, the most frequently used method remains the one involving measurement results from compression tests performed on multiple samples with different core angles [20–22].

Besides the adopted laboratory test schemes, the determination of accurate elastic constants is also influenced by the choice over suitable strain measurement techniques. In general, local strain measurements should preferably be used over global arrangements, such as cap-to-cap LVDT measurements. This is due to the influence of end-effects near the sample–platen contacts on the global measurements arising from surface friction [23]. To mitigate the influence of interface friction, Togashi et al. [24] proposed the use of a ball-bearing plate in between the sample's top surface and the loading platen within triaxial

tests on anisotropic rocks. However, the need for such a measure could not be confirmed by the study of Dambly et al. [25], who carried out uniaxial compression tests on granitic rocks with a specific degree of anisotropy.

The majority of studies in the literature dealing with the determination of the transversely isotropic elastic material constants involving uniaxial compression tests on cylindrical samples do not report the use of friction-reduction measures at the sample–platen contacts [13,14,20,21,26]. Nevertheless, the elastic parameters are calibrated by confronting the strain measurements containing the influence of end-effects with analytical strain equations derived from an ideal consideration. This introduces errors of uncertain magnitude into the determined elastic parameters compared to the true unaffected material constants of an assumed transversely isotropic elastic solid. In the current literature, it remains inadequately addressed to what extent the developing strain distributions around samples with different isotropy plane inclinations and the ascertainable material parameters are influenced by end-effects in combination with different inherent elastic constants. Uncertainty also exists as to whether friction-reducing measures are essential or dispensable in addition to local strain measurements in UCS tests on transversely isotropic rocks with varying elastic constants.

The present study aims to explore uncertainties through a theoretical perspective. It focuses on the determination of developing elastic strains around the circumference of cylindrical transversely isotropic rock specimens for the case of uniaxial compression loading. The influence of single material parameter variations in connection with varying anisotropy ratios E/E', ν/ν' and G/G', within observable ranges for low to moderately anisotropic rocks, is investigated. Analytical results are compared to the ones from numerical computations. In addition, the effects of more realistic test boundary conditions, which take into account sample–platen friction, are studied within numerical finite element simulations. The assessment addresses the associated influences on the generated strain distributions, as well as the results for the back-calibrated elastic constants. The originality of the study lies in the detailed graphical analysis of the impact that various study parameters exert on the results through the use of comprehensible polar diagrams. Another novel aspect is the identification of the influence of end-effects on the obtainable calibration results of the transversely isotropic constants based on the observed elastic deformation behavior of transversely isotropic rock specimens in numerical simulations of UCS tests.

In Section 2, the theoretical background to the analytical strain equations within the cylindrical coordinate system is provided. Further, the decisions made regarding the selection of suitable sets of elastic constants get justified and the approaches followed with regard to numerical modeling and the investigation of specimen end-effects are described. Section 3 presents and discusses the analytical and numerical results and makes a comparison between both. In addition, the quantitative influences of sample–platen contact friction on the calibration results are presented. A summary is provided in Section 4. The conclusions are drawn in Section 5.

2. Materials and Methods

2.1. Analytical Strain Equations in Cylindrical Coordinate System

As a matter of convenience, the present study adopts the same analogy for the parameter and coordinate system designations as Nejati et al. [16] and Dambly et al. [25]. For a transversely isotropic elastic solid, the stresses and strains are related via the generalized Hooke's law [11]. Referring to a local Cartesian $x'y'z'$ coordinate system, with the $x'y'$-plane coinciding with the material's isotropy plane orientation (see Figure 1), Hooke's law can be written as

$$
\underbrace{\begin{Bmatrix} \varepsilon_{x'} \\ \varepsilon_{y'} \\ \varepsilon_{z'} \\ \gamma_{y'z'} \\ \gamma_{x'z'} \\ \gamma_{x'y'} \end{Bmatrix}}_{\varepsilon'} = \underbrace{\begin{bmatrix} 1/E & -\nu/E & -\nu'/E' & 0 & 0 & 0 \\ & 1/E & -\nu'/E' & 0 & 0 & 0 \\ & & 1/E' & 0 & 0 & 0 \\ & & & 1/G' & 0 & 0 \\ & & & & 1/G' & 0 \\ & & & & & 1/G \end{bmatrix}}_{S'} \underbrace{\begin{Bmatrix} \sigma_{x'} \\ \sigma_{y'} \\ \sigma_{z'} \\ \tau_{y'z'} \\ \tau_{x'z'} \\ \tau_{x'y'} \end{Bmatrix}}_{\sigma'}
\tag{1}
$$

where ε' and σ' are the elastic strain and stress component vectors in Voigt notation and S' is the 6×6 transversely isotropic compliance matrix.
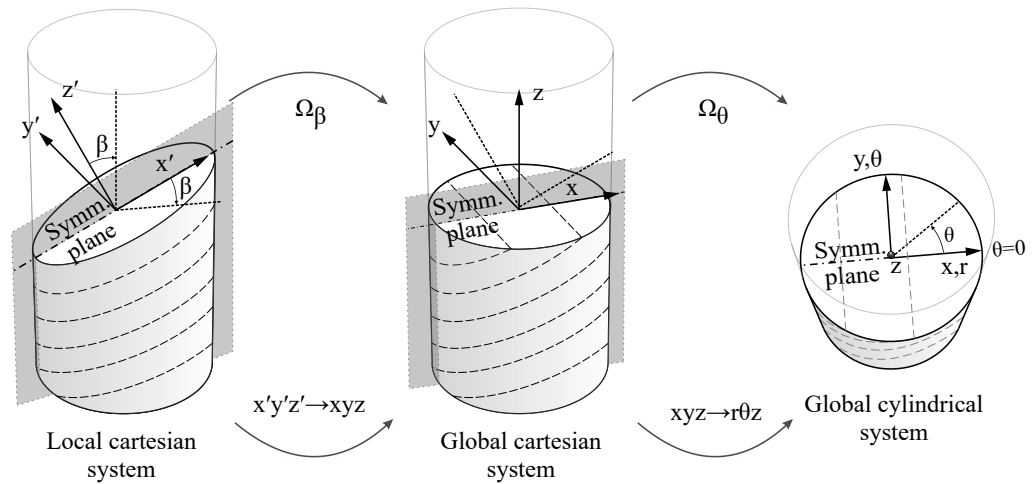
Figure 1. Transformation of the local Cartesian coordinate system $x'y'z'$ of a transversely isotropic cylindrical sample into the global cylindrical coordinate system $r\theta z$ in two steps using transformation matrices Ω_β and Ω_θ. The local x'-axis follows the inclination β of the isotropy planes within the sample's symmetry plane, which defines the direction $\theta = 0$ (based on Dambly et al. [25]).

In order to derive the analytical equations for the elastic strain components around transversely isotropic cylindrical samples subjected to uniaxial loading, two further coordinate systems are introduced, i.e., the global Cartesian xyz-system and the global cylindrical system $r\theta z$. The general loading configuration $\sigma = [0, 0, \sigma_z, 0, 0, 0]$ within the test and measurable normal strain components ε_r, ε_θ and ε_z around the cylinder are given within the latter system. Hence, to apply Hooke's law, the compliance matrix S' in Equation (1) needs to be transformed twice (using rotation matrices Ω_β and Ω_θ as described in Nejati et al. [16] and Dambly et al. [25]): first, from $x'y'z'$ to xyz, corresponding to a rotation around the y-axis; second, from xyz to $r\theta z$. Carrying out the transformations and assuming that the xz-plane is the sample's plane of deformational symmetry ($x \mathrel{\widehat{=}} \theta = 0$), the following equations for the normal strains ε_r, ε_θ and ε_z in relation to the isotropy plane inclination β in cylindrical coordinates are obtained [16,25]:

$$
\varepsilon_r = \left[\left(-\frac{\nu \sin^2 \beta}{E} - \frac{\nu' \cos^2 \beta}{E'} \right) \sin^2 \theta + \frac{1}{4} \left[\left(\frac{1}{E} - \frac{1}{G'} + \frac{1}{E'} \right) \sin^2 2\beta - \frac{\nu'(3 + \cos 4\beta)}{E'} \right] \cos^2 \theta \right] \sigma_z
\tag{2}
$$

$$
\varepsilon_\theta = \left[\left(-\frac{\nu \sin^2 \beta}{E} - \frac{\nu' \cos^2 \beta}{E'} \right) \cos^2 \theta + \frac{1}{4} \left[\left(\frac{1}{E} - \frac{1}{G'} + \frac{1}{E'} \right) \sin^2 2\beta - \frac{\nu'(3 + \cos 4\beta)}{E'} \right] \sin^2 \theta \right] \sigma_z
\tag{3}
$$

$$
\varepsilon_z = \left[\frac{\sin^4 \beta}{E} + \frac{\cos^4 \beta}{E'} + \frac{1}{4} \left(\frac{1}{G'} - \frac{2\nu'}{E'} \right) \sin^2 2\beta \right] \sigma_z
\tag{4}
$$

Equations (2)–(4) are exclusively valid under the assumption of a uniform axial stress state. This case is only satisfied for ideal test boundary conditions without interface friction between the sample and loading platens. Figure 2 illustrates the orientation of the acting normal strain components within the cylindrical coordinate system $r\theta z$.
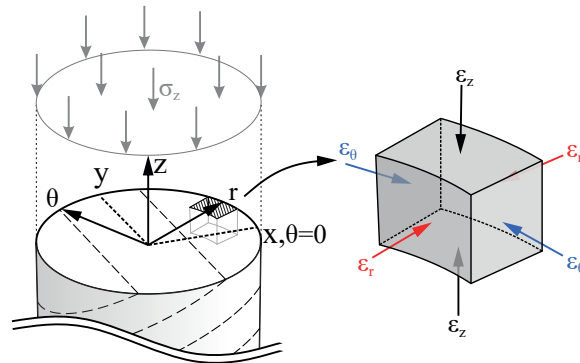
Figure 2. Local orientation of measurable normal strain components in the cylindrical coordinate system $r\theta z$ for uniaxial compression tests with frictionless boundary conditions. Strain component ε_θ is oriented in tangential direction to the sample circumference, ε_r in radial direction (based on Dambly et al. [25]).

2.2. Elastic Constants for Parametric Study

A parametric study carried out in the present paper aims at identifying the influence of individual material parameters on the developing elastic strains around transversely isotropic cylinders subjected to uniaxial loading. The considered parameter sets for the elastic constants were chosen based on commonly observed ranges and ratios for weak/moderately anisotropic rocks.

Typical values for anisotropy ratios E/E' and ν/ν' of transversely isotropic rocks were listed by Lama and Vutukuri [27]. Comprehensive studies on possible domains for these ratios referring to various rock types were carried out by Amadei et al. [5] and Worotnicki [28], their reviews largely relying on the parameter sets provided by Batugin and Nirenburg [29] and Gerrard [30]. The analyzed data in these studies not only include elastic constants from transversely isotropic rock samples but also orthotropic rock samples. In the latter case, the investigated Young's modulus ratio was taken as E_{max}/E_{min}, E_1/E_3, respectively, for comparative purposes with the E/E' ratio of rocks with rotational symmetry. Also, it should be noted that, in the study of Worotnicki [28], not only were static elastic constants analyzed but also dynamic constants.

2.2.1. Young's Moduli and Ratio E/E'

For the parametric study, the Young's modulus E' in direction normal to the isotropy planes was fixed with a value of 2000 MPa. This value can be considered to be arranged at the lower end of the values for the stiffness of various rock types, as could be encountered for fine-grained soft sedimentary rocks [31]. Also, this low value was chosen in agreement with the stiffness of artificial anisotropic samples that the authors are currently experimenting with. Keeping E' constant facilitates the investigation of the influence of stiffness anisotropy (E/E') on the qualitative strain distributions at consistent strain magnitudes. The Young's modulus E was made dependent on E' via the selected values for the anisotropy ratio E/E'.

For natural anisotropic rocks, the Young's modulus E' perpendicular to the planar fabrics is usually smaller than the Young's modulus E measured within the planes, with minor exceptions [5,27,32]. Thus, the lower bound for the selected E/E' ratio was chosen with 1.0. Amadei et al. [5] found that the majority of values for this ratio lie in between 1.0 and 2.0 based on 98 investigated rocks, with only a single case reported with a value larger than 3.0. From the frequency distributions shown in Figure 3, based on data collected

by Worotnicki [28] and Lama and Vutukuri [27], it can likewise be concluded that most of the rocks display low to moderate Young's modulus anisotropy ratios $E/E' < 2.0$. Nevertheless, Worotnicki's dataset (Figure 3a) is less balanced toward intermediate ratios, with 80% of the samples having ratios less than 1.5. This can be explained by the high amount of quartzofeldspathic and basic/lithic rocks included in the assessment usually displaying the lowest degrees of modulus anisotropy. In the given context of the parametric study, anisotropy ratios E/E' of 1.0, 1.5 and 2.0 were selected.
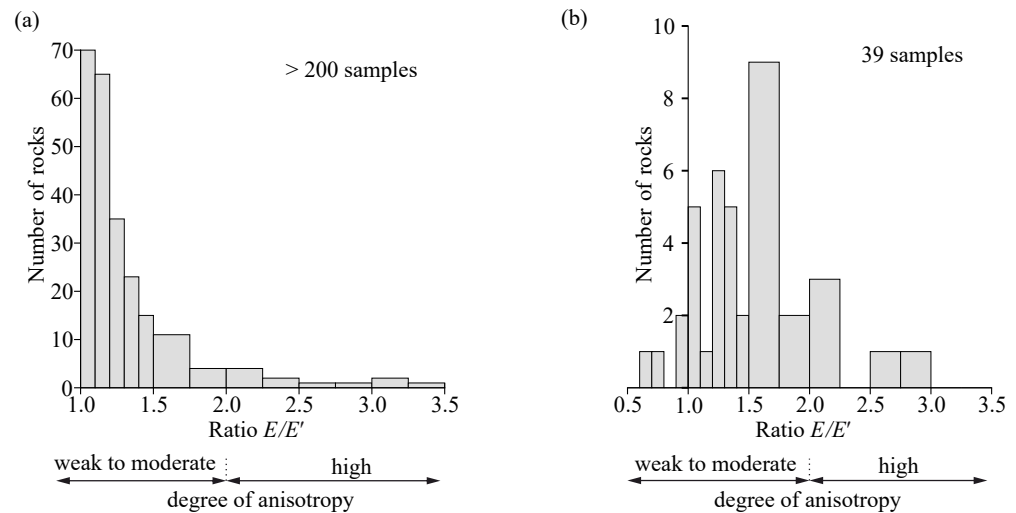
Figure 3. Frequency distribution of anisotropy ratios E/E' for various rock types as (**a**) studied by Worotnicki [28], including more than 200 samples in his study from 4 different lithological classes of anisotropic rocks and (**b**) as listed by Lama and Vutukuri [27]. In both datasets, rocks displaying exceptional values for anisotropy ratios greater than 3.5 were present, but were not considered in this figure due to the study's focus on weakly to moderately anisotropic rocks. The limit ratio sometimes defined in literature to distinguish weakly to moderately and highly anisotropic rocks is 2.0 [16].

2.2.2. Poisson's Ratios and Ratio ν/ν'

When considering a broad spectrum of rock types, typical values for Poisson's ratios range from numbers as low as 0.05 up to 0.4 [33]. However, certain quartz-rich sandstones and siltstones with open microcracks and -pores may even display auxetic material behaviors with negative values for the Poisson's ratios [34]. Values higher than 0.5 are also documented in the literature for anisotropic rocks, especially for the transverse Poisson's ratios ν' in highly anisotropic rocks [27]. Amadei et al. [5] reported the majority of values for $\nu_{12}(\widehat{=}\nu)$ of anisotropic rocks to fall in between 0.1 and 0.35, while $\nu_{13}(\widehat{=}\nu^*)$ varies to a larger extent from 0.1 to 0.7. The parameter ν^*, as used by Amadei et al. [5], is a different representation of the transverse Poisson's ratio ν', both of which are related via $\nu'/E' = \nu^*/E$. As stated by Sayers [32] for shales, the Poisson's ratio ν' can be smaller, larger or equal to the value of ν depending on existing inclusions of kerogen, microcracks or pores with a low aspect ratio and parallel orientation to the bedding planes.

Despite the wide ranges of possible values for the anisotropy ratio ν/ν', sometimes simplified assumptions are made in rock mechanics, such as $\nu/\nu' = E/E'$ [25]. A slightly different relationship is provided by the three-parameter formulation of the transversely isotropic stiffness matrix from Graham and Houlsby [35], requiring only three instead of five parameters to be calibrated. In this case, the relationship between the single parameter ratios is given by $\alpha = (E/E')^{1/2} = \nu/\nu' = G/G'$.

For the herein conducted parameter study, the transverse Poisson's ratio ν' was assumed to be constant with a value of 0.15. This was carried out to prevent excessively low values for ν when made dependent on ν' based on selected ratios ν/ν'. Considering chosen ratios for E/E' of 1.0, 1.5 and 2.0 and applying the above mentioned relationships,

let the authors come up with chosen values for ν/ν' of 0.5, 0.667, 1.0, 1.5 and 2.0. This corresponds to assumed values for ν from 0.075 to 0.3.

### 2.2.3. Shear Modulus G' and Saint-Venant Approximation

The shear modulus G' is the most laborious parameter to determine from the five independent elastic parameters of a transversely isotropic material [29]. The parameter G' may be determined directly in UCS tests on samples with inclined isotropy planes from the conduction of strain measurements at 45° to the cylinder axis [10,25]. Besides the direct determination, G' may likewise be obtained from the solution of the system of stress–strain equations arising from the transformed Hooke's law [2,14,36]. This requires the execution of multiple tests and measurements on commonly three samples with isotropy plane inclinations of $\beta = 0°$, $\beta = 90°$ and $\beta \neq 0°, 90°$.

Given the increased effort for the determination of the shear modulus G', in many practical applications, this parameter is approximated by G'_{sv} acc. to Equation (5).

$$G' \approx G'_{sv} = \frac{EE'}{E(1 + 2\nu') + E'} \tag{5}$$

This relationship, in the literature often referred to as the Saint-Venant approximation of the shear modulus, originates from the early studies of Saint-Venant [37] and is indicated here in the form of Lekhnitskii [11]. Although this approximation is frequently described as being purely empirical [2,38], it still relates to a theoretical background, as shown by Nejati et al. [16]. Through rotating the compliance matrix S', as well as stresses and strains from the local coordinate system $x'y'z'$ by an angle β around the y-axis (see Figure 4), with the y-axis oriented parallel to the isotropy plane's strike direction, the apparent shear modulus $G'_\beta \cong G_{xz}$ within the coordinate system xyz is related to the shear stress τ_{xz} and shear strain γ_{xz} by $\tau_{xz} = G'_\beta \gamma_{xz}$ with

$$\frac{1}{G'_\beta} = \underbrace{\left(\frac{1}{E} + \frac{1 + 2\nu'}{E'} \right)}_{G'_{sv}{}^{-1}} \sin^2(2\beta) + \frac{1}{G'} \cos^2(2\beta). \tag{6}$$
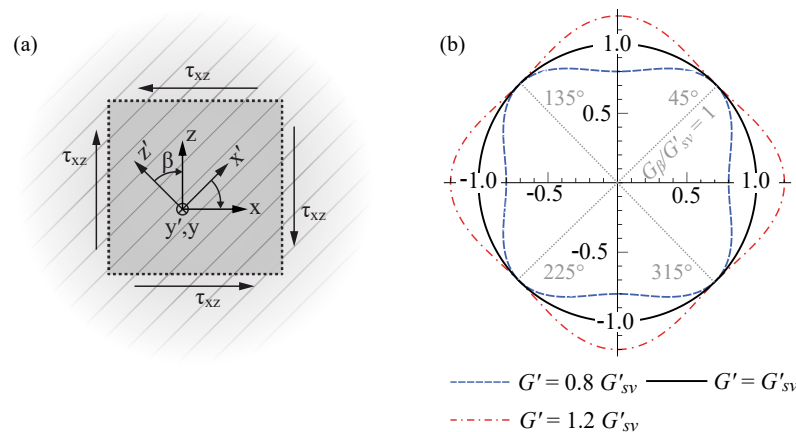
Figure 4. (**a**) Illustration of a quadratic cutout from a transversely isotropic solid oriented in the xyz coordinate system and subjected to shear stress τ_{xz}. (**b**) Polar plot of G'_β/G'_{sv} dependent on polar angle β and for varying values of the shear modulus G' assumed with 80, 100 and 120 % of G'_{sv} equal to unity (based on Nejati et al. [16]).

From Equation (6), it is obvious that, at angles $\beta = 45° + i \cdot 90°$, with i corresponding to any integer number, the apparent shear modulus G'_β equals the value from the approximation G'_{sv} due to the vanishing cosine term. This justifies the adoption of Equation (5) for simplification purposes, with deviations in the true to the approximated value of the shear modulus often

reported within a range smaller than 20% [16]. Emphasis should be given that this statement is only valid for rocks with low to moderate degrees of anisotropy, i.e., $E/E' < 2$.

For the parametric analytical study in this research, the shear modulus was taken as G'_{sv} acc. to Equation (5). To further investigate the influence of varying values for this elastic parameter on the developing strains, an additional value of $G'_{sv,Erat=2}$ computed at a ratio $E/E' = 2.0$ was additionally chosen for combinations with Young's modulus ratios smaller than 2. Numerical studies were conducted with values for the transverse shear modulus G' of $0.8 \cdot G'_{sv}$, G'_{sv} and $1.2 \cdot G'_{sv}$ considering commonly observed deviations from the approximated value G'_{sv}.

2.2.4. Parameter Sets and Stress Level

Table 1 lists all variation parameters as used for the analytical study on the developing strain distributions around a cylinder subjected to uniaxial compression loading. Based on these parameters, a total of 75 sets for the five elastic constants including varying values for the isotropy plane inclination β were studied. Among the elastic parameters, only the values for the Young's modulus E' and the Poisson's ratio ν' were fixed, with values of 2000 MPa and 0.15, respectively. From the selected constants and ratios, the satisfaction of the well-known thermodynamic constraints [5,39] for the elastic parameters of transversely isotropic materials is guaranteed. All strain distributions presented in the results section (Section 3) were computed for an assumed axial stress level σ_z of 10 MPa, whereby σ_z represents a linear scaling factor for the strain magnitude not influencing the qualitative strain distributions.

Table 1. Investigated parameters for analytical study.

Young's Modulus E' (MPa)	Poisson's Ratio ν' (-)	E/E' (-)	ν/ν' (-)	G' (MPa)	β (°)
2000	0.15	1.0, 1.5, 2.0	0.5, 0.667, 1.0, 1.5, 2.0	G'_{sv}, $G'_{sv,Erat=2}$	0, 45, 90

2.3. Numerical Studies

For the purpose of a graphical comparison with the analytical solutions for the strain distributions around cylindrical samples and to quantitatively asses the influence of sample–platen friction on the elastic strains, as well as on the back-calibrated elastic constants, numerical UCS test simulations were performed using the finite element software PLAXIS 3D CONNECT Edition V21 [40]. It was assumed that the samples undergo elastic deformations only without the consideration of plasticity. Failure conditions were only validated at the sample–platen interface where plastic deformations were permitted. This was performed to analyze the influence of frictional end-effects on the developing strain distributions around the cylinders at multiple horizontal cross sections acc. to Figure 5b. The platens were modeled as separate volume elements as can be seen in Figure 5.
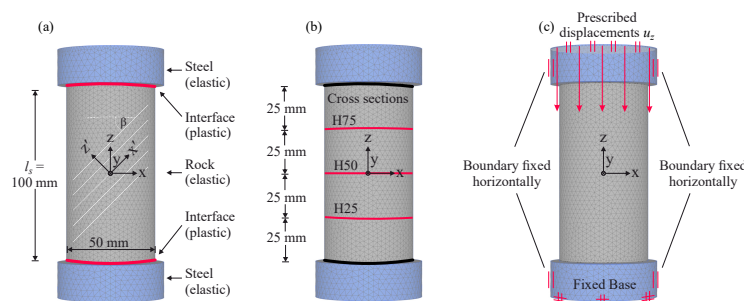

Figure 5. Illustration of the numerical model set-up for the uniaxial compressive strength (UCS) test simulation displaying (**a**) the general dimensions and chosen materials for the single model components, (**b**) the location and designation of horizontal cross sections used for the result evaluation and (**c**) the kinematic boundary conditions and the applied loading in terms of prescribed displacements u_z.

2.3.1. Model Description

The samples were modeled with a diameter of 50 mm and a height of 100 mm as shown in Figure 5a. The steel platen dimensions were taken into account as being 60 mm in diameter and 20 mm in height. Interface elements were placed between the sample and loading platens. Surfaces were located at 3 different positions along the sample volume at heights of 25 mm (H25), 50 mm (H50) and 75 mm (H75). This was performed in order to force mesh node positions at the intended cross sections, and thus to be able to evaluate the deformations at these locations. Figure 5b provides a graphical representation of the considered horizontal cross sections.

In addition, two surfaces were defined within the sample volume parallel to the *yz*- and the *xz*-plane and passing through the sample axis. These surfaces helped in achieving a higher mesh symmetry. In total, the mesh comprised 64,468 10-node tetrahedral elements and a number of 100,649 element nodes.

The steel material was modeled as elastic with an isotropic stiffness. For the rock material, the jointed rock (JR) model [40] was adopted. It considers elastic anisotropy by the implementation of a transversely isotropic stiffness matrix and plastic anisotropy by checking stresses against local Mohr–Coulomb failure criteria in implicit joint directions. In this study, any required input of strength parameters was chosen as sufficiently high to prevent yielding of the rock material. The interface on top and bottom of the sample was modeled using a Mohr–Coulomb constitutive model with zero cohesion. Two values for the friction angle of the interface were analyzed. The highest considered anisotropy ratio from the analytical study of $E/E' = 2$ was adopted for the rock samples within the numerical simulations. This was performed in accordance with the highest expected influence of sample–platen friction on the elastic strain distributions. Tables 2–4 provide an overview of the selected material parameters for the numerical simulations.

Table 2. Material parameters for the rock sample.

Parameter	Symbol	Value(s)	Unit
Young's modulus	E	4000	MPa
Poisson's ratio	ν	0.075, 0.1 *, 0.15, 0.225, 0.3	(-)
Young's modulus	E'	2000	MPa
Poisson's ratio	ν'	0.15	(-)
Shear modulus	G'	888 ($0.8G'_{sv}$), 1111 * (G'_{sv}), 1333 ($1.2G'_{sv}$)	MPa
Plane inclination	β	0, 45, 90	(°)

* Herein regarded as the "basis" parameter set.

Table 3. Material parameters for the steel platens.

Parameter	Symbol	Value	Unit
Young's modulus	E	200,000	MPa
Poisson's ratio	ν	0.3	(-)

Table 4. Material parameters for the interface between rock specimen and steel platens.

Parameter	Symbol	Value(s)	Unit
Young's modulus	E	20,000	MPa
Poisson's ratio	ν	0.3	(-)
Friction angle	φ	0, 15	(°)
Cohesion	c	0	MPa

With regard to the kinematic boundary conditions, all displacement components at the bottom boundary of the model were fixed. Movement at the vertical model boundary along the steel platens was only permitted in vertical direction and was locked in horizontal direction. The applied boundary conditions are presented in Figure 5c.

2.3.2. Load Application

The used finite element software is based on an implicit approach. Loading was applied uniformly on top of the upper loading platen in terms of prescribed displacements. In horizontal directions, the value of prescribed displacement was selected with zero. The value in vertical direction u_z, to be applied within the calculation phase, was determined by an iterative algorithm that was implemented via the *remote scripting interface* in PLAXIS 3D [40]. This measure was necessary for yielding the desired axial sample stress of 10 MPa, making the numerical results comparable to the analytical ones. A direct assumption for the value of prescribed vertical displacements was not possible due to the difficulties in assessing the influences of the interfaces together with the platen deformation.

The automated process for selecting the required value for the prescribed vertical displacements u_z included the determination of initial values using the following equation:

$$u_{z,init} = \frac{\sigma_{z,req}}{E_\beta} \cdot l_s, \tag{7}$$

with $\sigma_{z,req}$ equal to the considered axial stress level of 10 MPa, l_s corresponding to the sample height and E_β chosen as E' for $\beta = 0°$ and E for $\beta = 45°$ and $90°$.

After carrying out a first phase calculation, the *structural forces in volume piles* feature in PLAXIS was invoked to extract the axial force distribution along the sample axis, as shown in Figure 6a. The average axial stress $\sigma_{z,av}$ was determined by dividing the average axial force N_{av} by the sample cross section A_{cross}. From the averaged axial stress $\sigma_{z,av}$, the value for the prescribed vertical displacement u_z within a single loop was computed by multiplying the current value $u_{z,current}$ by the factor $\sigma_{z,req}/\sigma_{z,av}$. Using this newly determined value for u_z, the iterative procedure was continued until convergence of $\sigma_{z,av}$ to $\sigma_{z,req} = 10$ MPa, judged based on a small maximum tolerance, was reached and the final model results could be obtained. The whole iterative process is presented in a flow chart in Figure 6b.
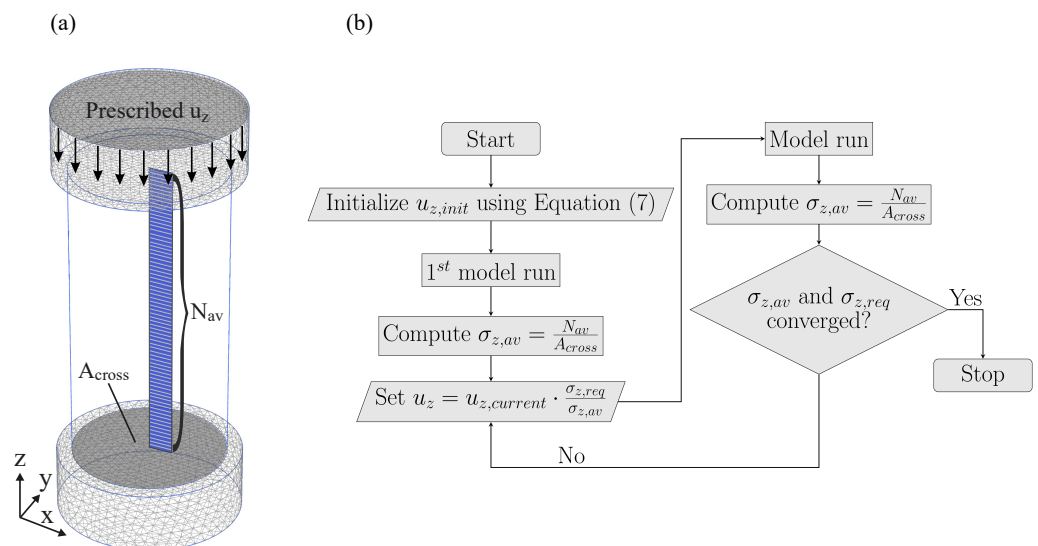

Figure 6. (**a**) Normal force distribution within the cylindrical sample with cross sectional area A_{cross} resulting from the applied loading in terms of prescribed displacement u_z. (**b**) Flow chart diagram describing the process of determining the value u_z to yield the required axial stress state $\sigma_{z,req}$ (in this study, 10 MPa).

2.3.3. Numerical Strain Evaluation

The resulting distributions for the radial strains ε_r and vertical strains ε_z from the numerical models were evaluated at the designated cross sections shown in Figure 5b.

The vertical strains ε_z were computed for pairs of vertically aligned circumferential mesh nodes at cross sections H25 and H75 ($P_{n,0(H25)}$ and $P_{n,0(H75)}$) from the relative change in vertical distance between these nodes. In total, 56 circumferential mesh nodes n were present in each of the considered cross sections. Figure 7a shows the distribution of these mesh nodes exemplary for cross section H75 besides the considered distances and length changes for the determination of the vertical strains ε_z. Referring to this figure, $\varepsilon_{z,n}$, corresponding to the vertical strain between a single pair of mesh nodes, can be calculated acc. to Equation (8).

$$\varepsilon_{z,n} = \frac{\Delta l_z}{l_{z,0}} \tag{8}$$
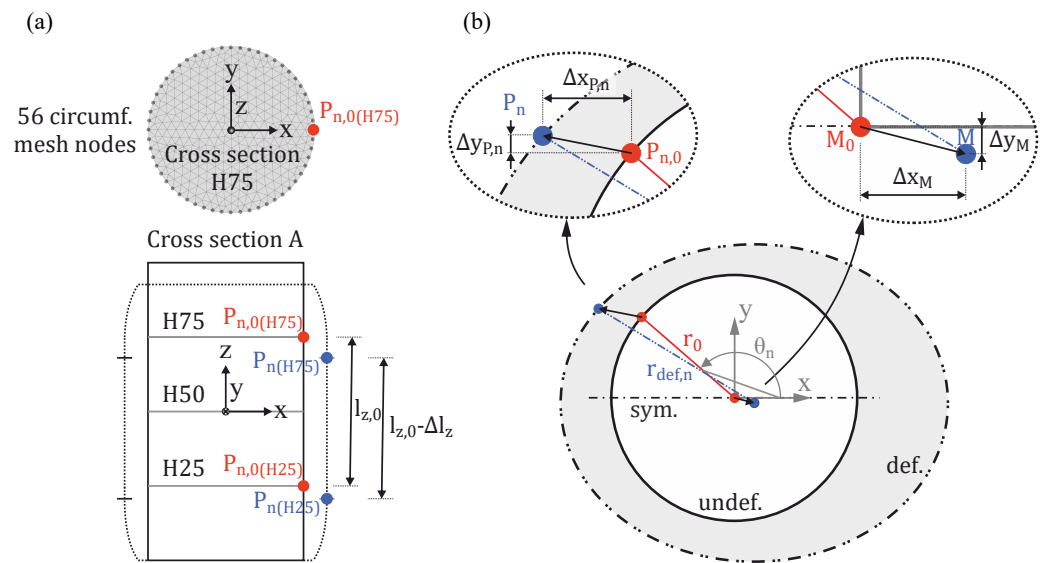
Figure 7. Sketch describing the considered point locations and length changes for the determination of the numerical circumferential distributions for (**a**) the vertical strain component ε_z evaluated between a single node pair $P_{n(H75)} - P_{n(H25)}$ (after Mutschler [41]) and (**b**) the radial strain component ε_r evaluated for a single circumferential mesh node oriented at θ_n positioned at a single cross section.

The determination of the radial strains ε_r around the cylindrical sample was carried out for each circumferential mesh node with orientation θ_n of each cross section individually. The absolute value for the radial strain corresponding to a single node n computes as

$$\varepsilon_{r,n} = \left| \frac{r_0 - r_{def,n}}{r_0} \right|, \tag{9}$$

where r_0 equals the initial radius of the sample and $r_{def,n}$ is computed as the horizontal distance between the deformed nth circumferential mesh node and the shifted center point M of the individual cross section. Figure 7b displays the considered point displacements used to derive the deformed distance $r_{def,n}$ for a cross sectional mesh node oriented at θ_n and located at the sample circumference.

2.3.4. Back-Calibration of Elastic Constants

To quantify the potential influence of sample–platen friction on the measurable elastic strain components and further on the calibration results for the transversely isotropic parameters, a back-calibration of the secant values of the elastic constants as considered within the numerical simulations was carried out at the specified stress level of 10 MPa. Thereby, the simulated strain distribution curves at the central cross section H50 (Figure 5b), the discrete strain values along the x- and y-axis, respectively, were regarded as the measurements as usually received from actual tests. From a comparison of the numerical and analytical strains computed for consistent parameter sets (Table 2), no visual differences in

the strain distributions were encountered at the inspected central cross section for samples with isotropy plane inclinations of $\beta = 0°$ and $90°$. Thus, the assumption is made that, given that the standard evaluation procedure for the elastic constants from local strain measurements is applied [10], which derives parameters E' and ν' exclusively from a test on a sample with $\beta = 0°$ and E and ν from a test on a sample with $\beta = 90°$, the respective parameters remain unaffected by the influence of sample–platen friction. Consequently, only the effects of interface friction on the back-calibrated transverse shear modulus G' were investigated. This was performed by evaluating the numerical results for the radial strain components ε_r in x-axis direction ($\theta = 0°/180°$) and deriving the value for G' from Equation (2).

3. Results and Discussion

In the following, the resulting strain distributions around transversely isotropic cylindrical rock samples subjected to a uniaxial compressive stress of 10 MPa are presented. In the first step, the analytical results, using parameter combinations as listed in Table 1, are demonstrated. Subsequently, the numerical results for a rock sample with the "basis" parameter set acc. to Table 2 are visually compared to the analytical solutions. Additionally, the potential effects of sample–platen friction on UCS test calibration results are quantified based on evaluating the differences between the back-calibrated values for the transverse shear modulus G' and the value as used in the numerical models. Elastic parameter sets as listed in Table 2 are considered in this regard. As can be seen from Figure 8a,b, the distributions for the radial and circumferential strains, ε_r and ε_θ, around a transversely isotropic cylinder under uniaxial loading only differ in terms of a phase shift of the curves by 90° with the otherwise same absolute values. Consequently, the authors only present the radial and vertical strain distributions in the results section. All considered strain values are plotted with their absolute values only, being well aware that axial sample strains result in a shortening of the sample axis and that the lateral strains yield an extension of the specimen for the herein considered values of the elastic parameters.
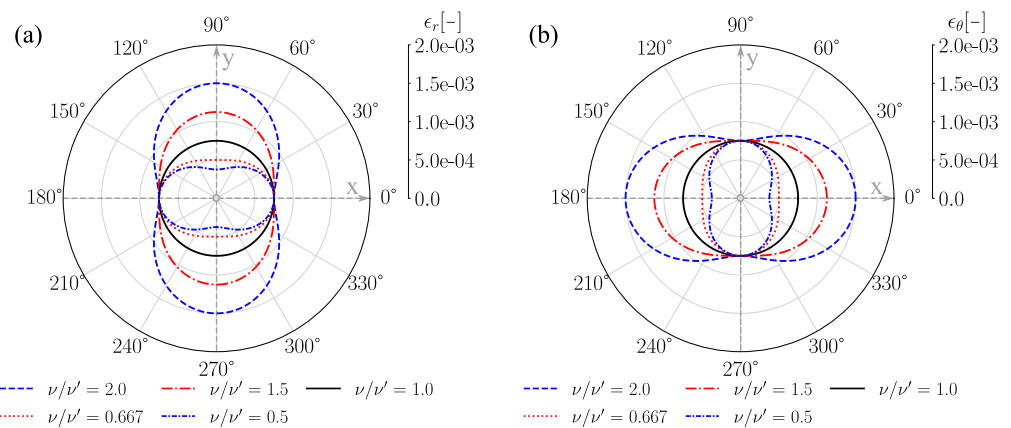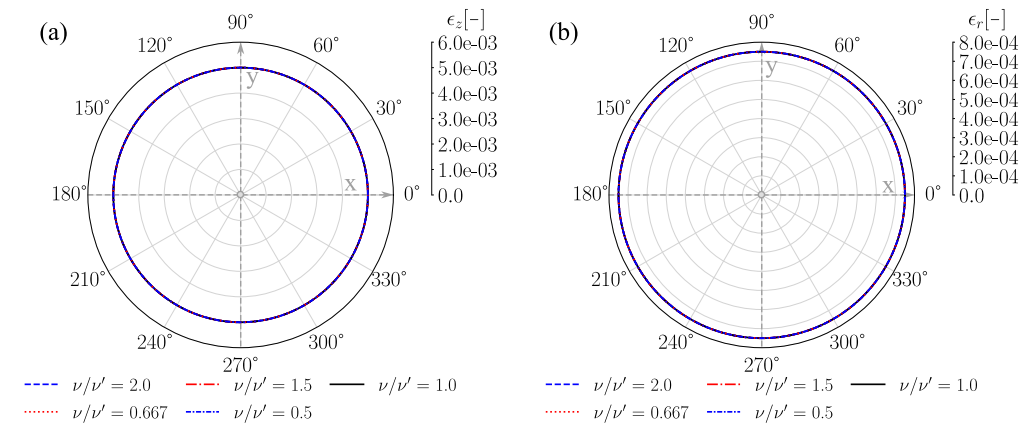

Figure 8. Analytical strain distributions plotted in a range of $\theta = 0°$ to $360°$ for a chosen parameter set acc. to Table 1 with $E/E' = 1.0$, a shear modulus of $G' = G'_{sv,Erat=2} = 1111$ MPa and a dip angle $\beta = 90°$ using various ratios ν/ν': (**a**) radial strains ε_r and (**b**) circumferential strains ε_θ representing a 90° phase shift of the radial strain curves.

3.1. Analytical Results

The analytical results for samples with horizontal isotropy planes ($\beta = 0°$) are presented in Section 3.1.1. Sections 3.1.2 and 3.1.3 discuss the influences of single elastic parameters on the developing radial strains ε_r and the vertical strains ε_z respectively, for samples with inclined ($\beta = 45°$) and vertical isotropy planes ($\beta = 90°$).

3.1.1. Samples with Horizontal Isotropy Planes

As a result of the chosen study parameters, with the elastic constants E' and ν' assumed with fixed values, the resulting radial and vertical strains, ε_r and ε_z, for samples with an isotropy plane inclination of $\beta = 0°$ are not affected by the varied ratios E/E' and ν/ν'. Also, they remain unaffected by the shear modulus G'. For samples with horizontal isotropy planes, the only elastic parameters contributing to the developing strains ε_r and ε_z at orientation angle θ are E' and ν'. Figure 9 presents the results for the strain distributions associated with samples having an isotropy plane inclination of $\beta = 0°$.

Figure 9. Analytical strain distributions for samples with isotropy plane inclination $\beta = 0°$ plotted in a range of $\theta = 0°$ to $360°$ for various ratios ν/ν': (**a**) vertical strains ε_z and (**b**) radial strains ε_r. Obviously, no dependency on ratios E/E', ν/ν' or the shear modulus G' is given.

### 3.1.2. Influence of Elastic Parameters on Radial Strain Distributions

For plane inclinations different from $\beta = 0°$, the resulting radial strain curves are influenced by the ratios E/E' and ν/ν'. Additionally, the shear modulus G' influences the cases with $\beta = 45°$. Figure 10 displays the radial strain distributions in dependency of ratios E/E' and ν/ν' for samples with plane inclinations β of $45°$ and $90°$. The curves are depicted for a constant value of G' selected as $G'_{sv,Erat=2}$ computed for a ratio $E/E' = 2$ using Equation (5).

It can be seen that increasing ratios ν/ν', corresponding to an increase in the Poisson's ratio ν, result in increased radial strains in the vicinity of the y-axis with vanishing influence toward the x-axis. This statement holds independently of the investigated ratios E/E' and isotropy plane inclinations of $\beta = 45°$ and $90°$. The radial strains on the x-axis, which corresponds to the samples' symmetry plane, remain unaffected by changing values of ν.

At constant ratio E/E' with fixed values for the Young's moduli and $\beta = 45°$, the only two parameters influencing the radial strains along the x-axis are Poisson's ratio ν' and the transverse shear modulus G'.

For $\beta = 90°$, the shear modulus G' does not affect the resulting strains. The radial strains along the x-axis are exclusively determined by the parameters ν' and E'. As both parameter values are fixed for the curves shown in Figure 10, the values for the radial strains along the x-axis from curves with constant ratio E/E' do not differ.

For cases with $\beta = 45°$, increasing values for the Young's modulus E for otherwise constant elastic parameters leads to a reduction in the radial strains in the vicinity of the y-axis. The strains along and close to the x-axis increase. For samples with an isotropy plane inclination of $\beta = 90°$, only the strains toward the y-axis direction are affected by varying values for the Young's modulus E.
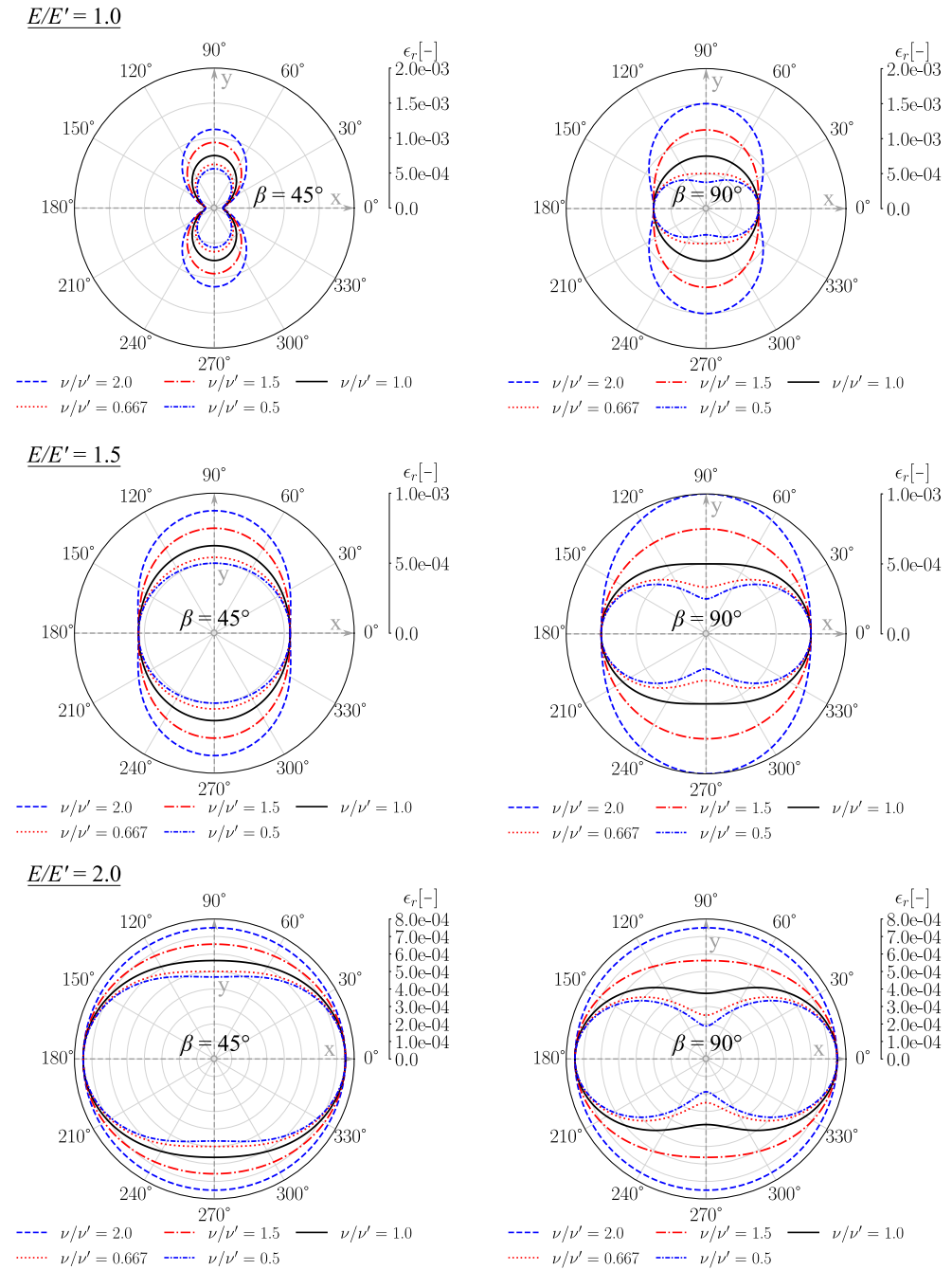
Figure 10. Distributions of radial strains ε_r for samples with dip angles $\beta = 45°$ and $90°$, ratios E/E' of 1.0, 1.5 and 2.0 and a constant shear modulus $G' = G'_{sv,Erat=2} = 1111$ MPa displayed within a range of $\theta = 0°$ to $360°$ and plotted for various ratios ν/ν'.

It holds that, for samples with isotropy plane inclinations of $\beta = 90°$, uniform radial strain distributions are obtained in the case of equal ratios E/E' and ν/ν'. For samples with $\beta = 45°$ and $E/E' = \nu/\nu'$, the uniformity of radial strains is only guaranteed when, additionally, the shear modulus is equal to G'_{sv} derived from the approximation provided by Equation (5). In Figure 10, this is only the case for the curve with $E/E' = \nu/\nu' = 2.0$, since all curves from this figure result from computations with a constant shear modulus $G' = G'_{sv,Erat=2}$ evaluated for a ratio E/E' of 2.0. Under this assumption, for the shear modulus G', uniform radial strains at any other ratio E/E' are only satisfied for specific values K of the ratio ν/ν' acc. to Equation (10). An example is given by the curve in Figure 10 with $E/E' = 1.5$, $\nu/\nu' = 0.667$ and $\beta = 45°$.

$$K = \frac{E(1 + 4\nu') - 2E'}{4E'\nu'} \tag{10}$$

Equation (10) is derived from plugging in Equation (5), with E expressed as $2E'$, into Equation (2), assuming β with $45°$ and equalizing the terms that are multiplied by $sin^2\theta$ and $cos^2\theta$.

The influence of shear modulus G' on the developing radial strains for cases with E/E' of 1 and 1.5 and angle $\beta = 45°$ can be seen when comparing Figure 10 with Figure 11. The curves in Figure 11 are depicted for a shear modulus selected as G'_{sv} acc. to Equation (5) in dependency of E and the fixed values for E' and ν'. From changing the values for the shear modulus, the strains along the y-axis remain unchanged, while the strains in other directions change with increasing rates toward the x-axis orientation. When selecting G' as G'_{sv}, the radial strains along the x-axis show no more dependency on the ratio E/E'. Thus, the same values for the x-axis strains are received for all curves with different ratio E/E' from Figure 11 and the curve with $E/E' = 2$ and $\beta = 45°$ from Figure 10. The absolute value for the radial strains along the x-axis in these cases is given by $\varepsilon_{r,x} = (\nu'/E') \cdot \sigma_z$. This expression is derived from inserting $G' = G'_{sv}$ acc. to Equation (5) into Equation (2) and simplifying the expression for considered angles of $\beta = 45°$ and θ of $0°$ or $180°$.
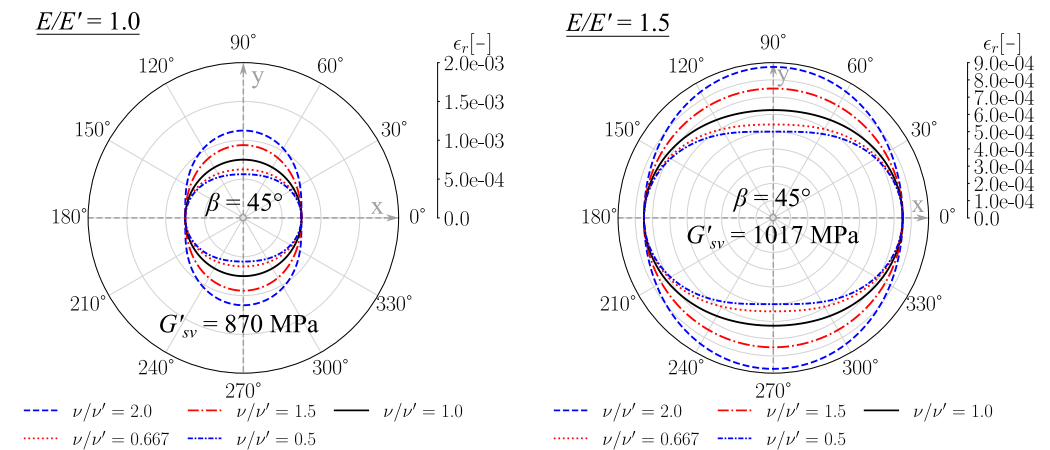

Figure 11. Distributions of radial strains ε_r for samples with dip angles $\beta = 45°$, ratios E/E' of 1.0, 1.5 and a shear modulus $G' = G'_{sv}$ acc. to Equation (5) displayed within a range of $\theta = 0°$ to $360°$ and plotted for various ratios ν/ν'.

3.1.3. Influence of Elastic Parameters on Vertical Strain Distributions

The analytical vertical strains as computed from Equation (4) are independent of the orientation θ. For the investigated cases including various plane inclinations, the vertical strains do not have a dependency on the ratio ν/ν' since varying ratios only correspond to a change in Poisson's ratio ν. However, this parameter is not part of the vertical strain equation. In contrast, the transverse Poisson's ratio ν', which actually affects the vertical strains, remains unchanged for all considered parameter sets.

For samples with horizontal isotropy planes, i.e., $\beta = 0°$, the vertical strains are received from $\varepsilon_z = (1/E') \cdot \sigma_z$ and are therefore only dependent on the elastic parameter E', which is fixed in this study. The resulting strain distribution for this case can be seen in Figure 9a.

For isotropy plane inclinations of $\beta = 90°$, the vertical strains can be computed from $\varepsilon_z = (1/E) \cdot \sigma_z$ and are only influenced by the Young's modulus E. Accordingly, only the chosen ratios for E/E' have an effect on the vertical strains for this plane inclination (see Figure 12a).
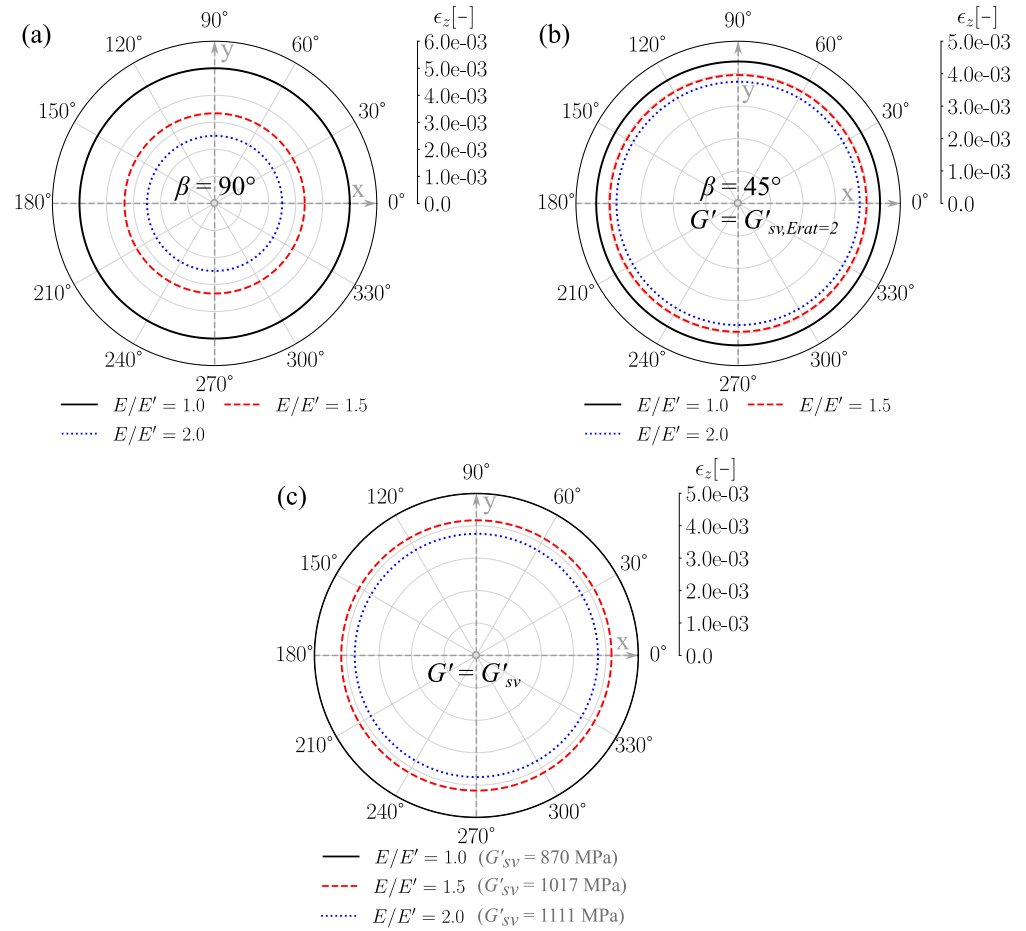
Figure 12. Distributions of vertical strains ε_z for samples with varying ratios E/E' and (**a**) an isotropy plane inclination of $\beta = 90°$, without an influence of the shear modulus, (**b**) with $\beta = 45°$ and a shear modulus of $G' = G'_{sv,Erat=2} = 1111$ MPa and (**c**) with $\beta = 45°$ and a shear modulus of $G' = G'_{sv}$ depending on the ratio E/E'.

When the plane inclination β is equal to 45°, the shear modulus G' has an influence on the developing vertical strains ε_z, which can be seen from Figure 12b,c. The curves in Figure 12b are plotted using a constant value for the shear modulus $G' = G'_{sv,Erat=2}$ computed at ratio $E/E' = 2.0$. Inserting the expression for G'_{sv}, following Equation (5) with $E = 2E'$, into Equation (4) results in a vertical strain value for samples with $\beta = 45°$ of $\varepsilon_z = [(2E' + 5E)/(8EE')] \cdot \sigma_z$. No direct dependency on the Poisson's ratios ν and ν' is given.

When the shear modulus G' is chosen as G'_{sv} acc. to Equation (5) considering the corresponding ratio E/E' (see Figure 12c), the vertical strain value for samples with isotropy plane inclination $\beta = 45°$ computes as $\varepsilon_z = [(E' + E)/(2EE')] \cdot \sigma_z$. Thus, differences in the results from Figure 12b,c occur; however, this is only for the curves with $E/E' \neq 2.0$.
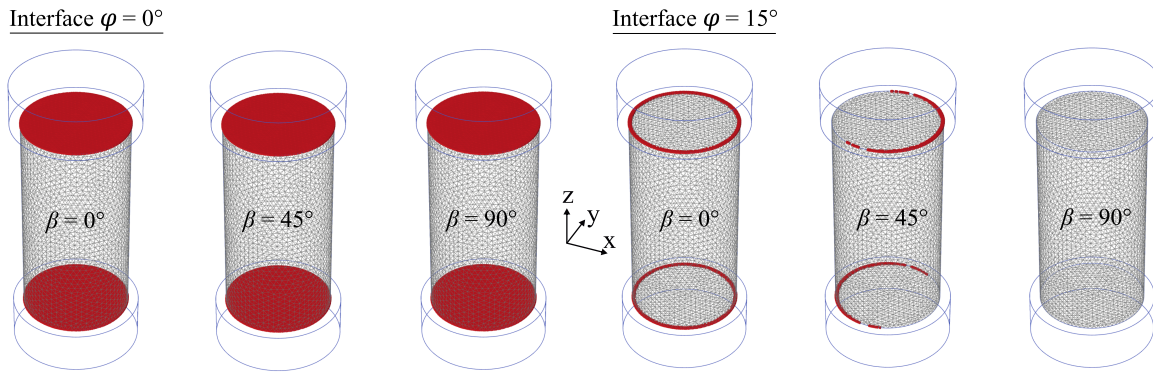
3.2. Numerical Results

The simulation results for the models with an interface friction angle of $\varphi = 0°$ show that the analytical solutions can be reproduced numerically regardless of the considered cross sections acc. to Figure 5b. Differences to the analytical results for the strain distributions can only be recognized with respect to the results from the models with a higher interface friction angle of $\varphi = 15°$.

3.2.1. Interface Plastic Points

From the selection of the corresponding interface friction angles with values of $\varphi = 0°$ and 15°, the desired two cases for the interface behavior are achieved:

1. Full plastification of the interface for $\varphi = 0°$, representative of the ideal case without any end-effects on the loaded sample.
2. Partial to no plastification of the interface with $\varphi = 15°$, representative of the realistic case with influencing end-effects.

The obtained plastic points for models based on the "basis" parameter set (see Table 2) with varying values of the interface friction angle φ and isotropy plane inclinations β are depicted in Figure 13.

Figure 13. Exemplary numerical results for the plastic points at the interfaces between sample and platens for various isotropy plane inclinations β and interface friction angles φ of $0°$ and $15°$.

3.2.2. Sample Deformations

Resulting from the assumed values for the elastic parameters of the rock material, sample deformations, where an example is shown in Figure 14 for the "basis" parameter set acc. to Table 2, occur due to the uniaxial compression loading of 10 MPa. Under non-restrained conditions with $\varphi = 0°$, the sample theoretically undergoes uniform vertical displacements. The restraining effect of any interface friction at the sample–platen contact results in the non-uniformity of the vertical sample displacements.
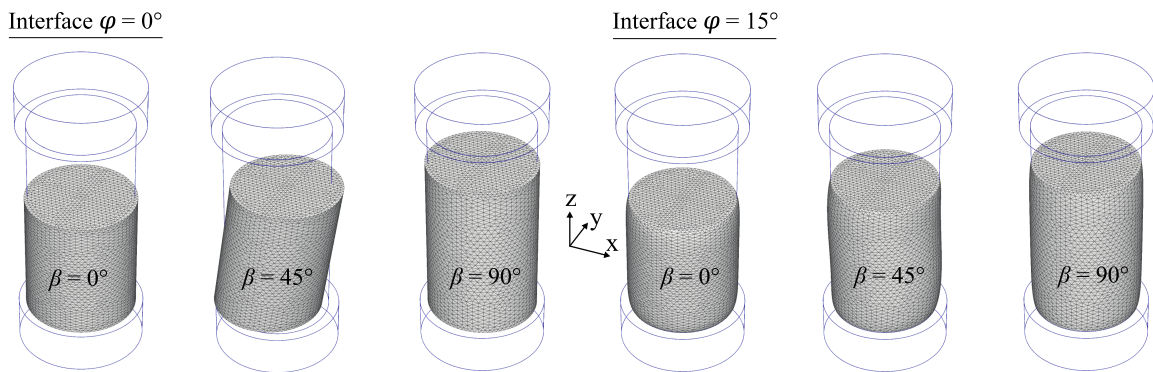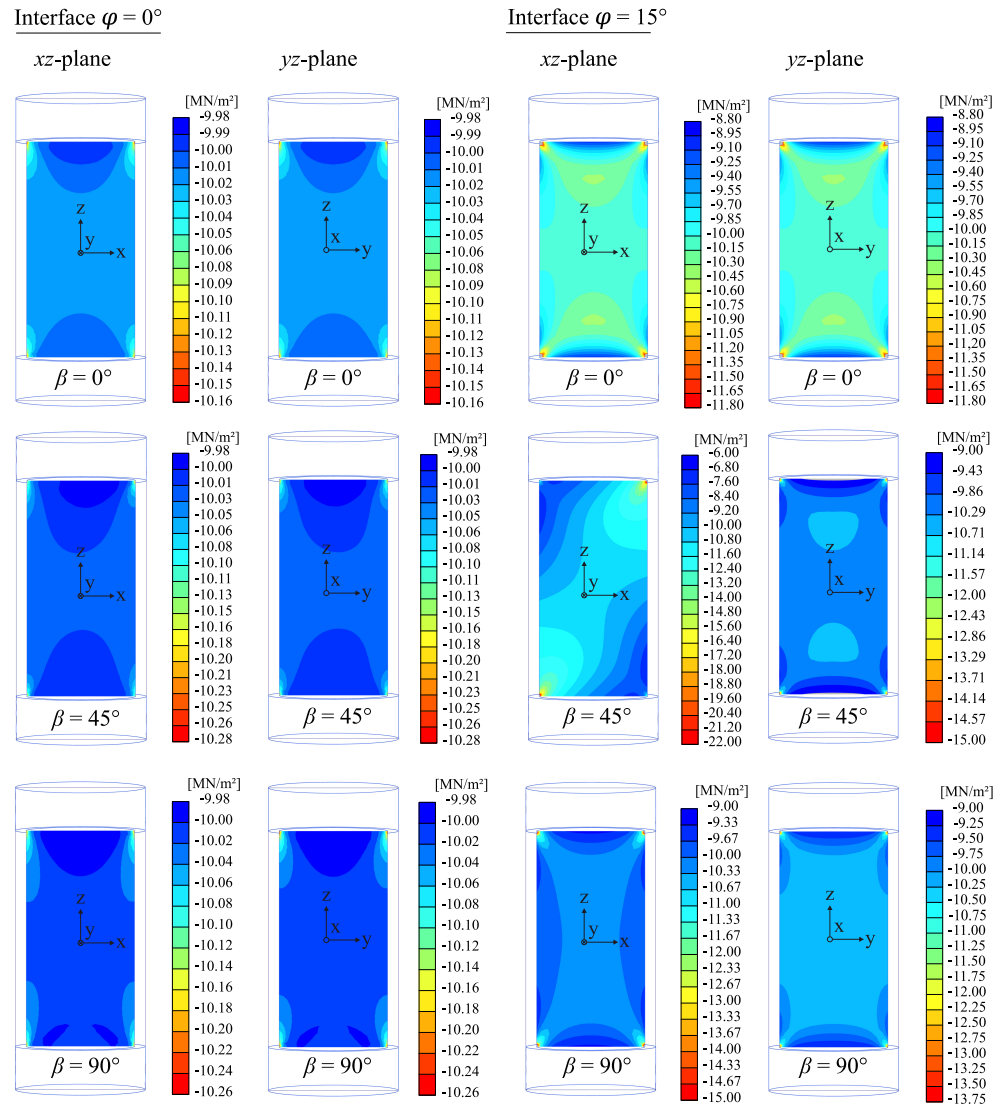

Figure 14. Exemplary numerical results for the deformed meshes of models with various isotropy plane inclinations β and interface friction angles φ of $0°$ and $15°$ (scaling factor = 80).

From a theoretical point of view, axisymmetric conditions with regard to deformations are only reached for samples with horizontal plane inclinations ($\beta = 0°$). For any other value of β, axisymmetry is not retained. However, planar symmetry in the deformations is still acquired around the sample's symmetry plane, which corresponds to the plane xz as shown in Figure 1.

3.2.3. Vertical Stress Distributions

Figure 15 displays the simulation results for the axial stress distributions for models with various isotropy plane inclinations β and interface friction angles φ considering the

"basis" parameter set acc. to Table 2. It is apparent from this figure that stresses close to the uniaxial state are only reached for the models with an interface friction angle of $\varphi = 0°$. The small divergences from the uniaxial stress state are mainly related to difficulties of the finite element solution in approximating the solution at re-entrant corners of the domain [42]. At such locations, singularities arise. It is also noticeable that, as a result of the skewing of the sample with $\beta = 45°$, slightly asymmetric stress distributions within the depicted planes arise.
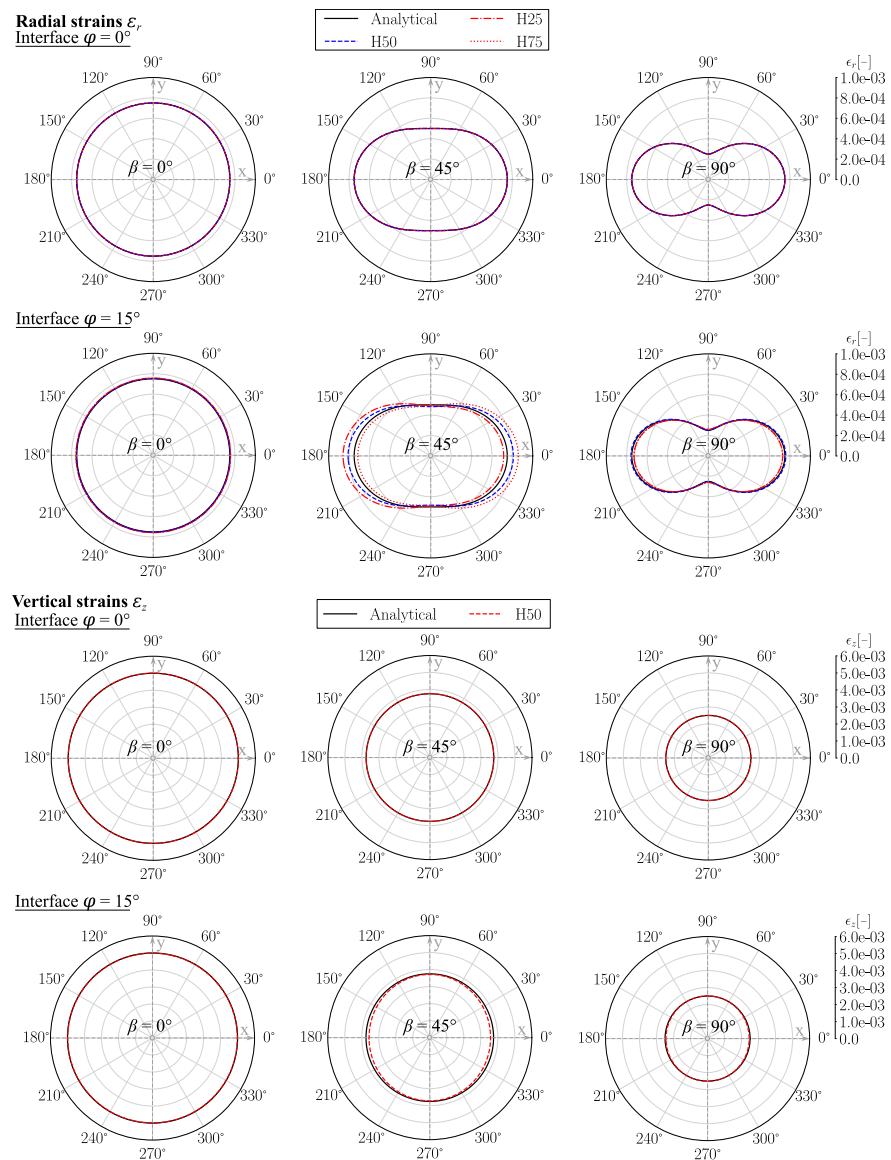

Figure 15. Numerical results for the vertical stresses σ_z along the planes xz and yz for models with various isotropy plane inclinations β and interface friction angles φ of 0° and 15°.

Selecting an interface friction angle φ of 15° introduces forced stresses into the specimens as the lateral movements at the top and bottom surfaces get restrained. Stress concentrations are visible at the top and bottom edges of the samples as already observed by Wei and Chau [43], who derived an analytical solution for stresses and displacements of transversely isotropic elastic cylinders under compression with end-effects. The biggest difference in comparison with the non-restrained cases ($\varphi = 0°$) is recognizable for the resulting xz-plane stresses from the model with $\beta = 45°$. In this case, larger stress inhomogeneities, especially in the inner third of the sample, are more visible than in other models. Ideally, however, homogeneous local stresses are desired in this region of the specimens, since this is where the local axial and radial strain measurements are usually carried out.

In general, planar symmetry of the developing stresses with respect to the plane *xz*, which is the samples' symmetry plane (see Figure 1), is visible. A different visual observation can only be made for the model with $\varphi = 0°$ and $\beta = 45°$, although the stress variability in this model is marginal and the cause is rather related to inaccuracies in the finite element approximation.

3.2.4. Comparison of Numerical and Analytical Results

Figure 16 provides a comparison of the resulting strain distributions from the numerical models, considering the basis parameter set acc. to Table 2, with the analytical solution. It is observed that, for the numerical models with an interface friction angle of $\varphi = 0°$, an almost perfect fit for the resulting radial (ε_r) and vertical (ε_z) strain distributions with the analytical solution is achieved. This clearly demonstrates that the chosen approach for inducing the required axial stress level of 10 MPa within the simulations is sufficient. Also, the selected procedure for the determination of the axial and vertical strains from the numerical models seem to provide reliable results.

Figure 16. Comparison of the numerical and analytical results for the radial and vertical strains, ε_r and ε_z, evaluated at specific cross sections H# for various isotropy plane inclinations β and interface friction angles φ.

The boundary effects caused by friction between the sample and platens have a negligible effect on the resulting strain distributions at the central cross section H50 for the models with $\varphi = 15°$ and isotropy plane inclinations β of 0° and 90°. From the resulting radial strains ε_r of the model with $\beta = 45°$ and $\varphi = 15°$, it is evident that the distributions at cross sections H25 and H75, closer to the boundaries, take on asymmetric shapes. Values from the curves associated with these two cross sections show the biggest divergence from the analytical solution in the x-axis direction. At the sample's central cross section H50, symmetry in the radial strain curve is kept. Nevertheless, deviations from the analytical solution are still visible and are largest again in the direction of the x-axis.

The specific direction for the occurrence of the largest deviation from the analytical solution was confirmed along the x-axis for samples with $\beta = 45°$ from further simulations considering the extended parameter sets acc. to Table 2. This suggests that, for moderately anisotropic rocks with E/E' of ~2, the transverse shear modulus G' is the elastic calibration parameter affected the most by interface friction when calibrated based on the corresponding radial strain measure.

Regarding the distributions of vertical strains ε_z in Figure 16, it can be seen that the influence of interface friction is only visible in terms of a slight non-uniformity in the generated distribution for the sample with $\beta = 45°$. However, as vertical strains are usually evaluated as a single averaged value from multiple local measurements around the central cross section, the small deviations can be considered negligible for practical purposes.

3.2.5. Influence of Interface Friction on Calibrated Elastic Parameters

Following the assumptions of Section 2.3.4 and the observations made in Section 3.2.4, the influence of an arising friction at the interface between the sample and platens on the generated strain distributions at the central cross section for samples with $\beta = 0°$ and 90°, and thus on the calibration results for parameters E, E', v and v', is considered negligible.

Table 5 shows the analytical and numerical values for the radial strain components ε_x in the x-direction as received at the central cross section for samples with $\beta = 45°$, considering an interface friction of $\varphi = 15°$ and the corresponding elastic parameter sets. Further, the back-calibrated values for the transverse shear modulus G' from the numerical solutions and the percentage differences between the analytically and numerically derived strains ε_x, as well as the back-calibrated and applied values for G', are listed.

Table 5. Comparison . of analytical and numerical values for radial strains in x-direction and influence of interface friction on the numerical calibration results for G'.

		Elastic Parameter Sets					Results		
E'	v'	E/E'	G'	v/v'	ε_x (Equation (2))	ε_x (Num.)	G' (Backcal.)	$\Delta\varepsilon_x$ [%]	$\Delta G'$ [%]
				2	3.75×10^{-4}	4.23×10^{-4}	1299.78	12.91	−2.51
				1.5	3.75×10^{-4}	4.26×10^{-4}	1298.02	13.60	−2.64
			1333	1	3.75×10^{-4}	4.29×10^{-4}	1296.24	14.31	−2.77
				0.667	3.75×10^{-4}	4.30×10^{-4}	1295.02	14.79	−2.86
				0.5	3.75×10^{-4}	4.31×10^{-4}	1294.41	15.04	−2.91
				2	7.50×10^{-4}	8.03×10^{-4}	1085.36	7.12	−2.31
				1.5	7.50×10^{-4}	8.06×10^{-4}	1084.20	7.45	−2.41
2000	0.15	2	1111	1	7.50×10^{-4}	8.08×10^{-4}	1083.02	7.78	−2.52
				0.667	7.50×10^{-4}	8.10×10^{-4}	1082.22	8.01	−2.59
				0.5	7.50×10^{-4}	8.11×10^{-4}	1081.81	8.13	−2.63
				2	1.31×10^{-3}	1.375×10^{-3}	869.44	4.99	−2.18
				1.5	1.31×10^{-3}	1.378×10^{-3}	868.66	5.19	−2.27
			888	1	1.31×10^{-3}	1.381×10^{-3}	867.89	5.39	−2.35
				0.667	1.31×10^{-3}	1.382×10^{-3}	867.37	5.52	−2.41
				0.5	1.31×10^{-3}	1.383×10^{-3}	867.11	5.58	−2.44

The results indicate that, for moderately anisotropic rocks (E/E'~2), the generated elastic radial strains in the x-direction under realistic UCS test conditions, i.e., with friction between samples and platens, are mainly influenced by the inherent transverse shear

stiffness of the material and the degree of anisotropy of the Poisson's ratios (ν/ν'). The largest differences between analytical and numerical strains exist for samples with high inherent shear moduli and low ratios ν/ν'. However, while the numerical strain values at a load level of 10 MPa, associated with simulated friction at the sample–platen contact, show deviations from the analytical solutions of up to 15.04 %, the effects on the back-calibrated values for the shear moduli are only in the range of maximum ~3%. This deviation can be considered as practically irrelevant, and higher errors might be associated with material heterogeneity and the natural variability between multiple samples.

4. Summary

The behavior of transversely isotropic rock specimens can be quite complex even in seemingly simple loading scenarios such as uniaxial compression. In this paper, we therefore investigated the influence of single transversely isotropic parameters on the elastic strain distributions around cylindrical rock specimens using an analytical solution to the problem of uniaxial compression. Basic parameter sets were derived from naturally observed ranges for the elastic parameters of rocks with transversely isotropic behavior. The results from finite element simulations, deploying a specific set of elastic constants, were compared to the analytical reference. An iterative method for generating the desired global uniaxial stress level in terms of applied prescribed displacements and a suitable procedure for the strain evaluation were presented. Additionally, the effect of interface friction between the sample and loading platens was studied in terms of the potential effects on stress heterogeneity, resulting strain distributions and calibration values for the elastic parameters.

5. Conclusions

Based on the conducted studies summarized in Section 4, the chosen representation for the investigated strain curves in terms of polar diagrams for specimens with different isotropy plane inclinations proved to be suitable for depicting the influences of different elastic parameters. Confronting such curves, based on calibrated elastic parameters, with the actual strain measurements can also be useful to identify inaccurate measurements and outliers in practice. Non-uniform radial strain distributions are generally obtained for transversely isotropic samples. Only for the case of horizontal planes of isotropy or specific combinations of the elastic constants and ratios between them is strain uniformity reached. From visual inspections of the generated strain distributions, it is evident that the gradients of the strain curves for parameter sets resulting in concave shapes are highest in the vicinity of strain measures along the x- and y-axis, as usually considered for the calibration of the elastic constants. This underlines the significance of the precise positioning of strain gauges and/or measurement extensometers to prevent substantial inaccuracies in the calibration results for the elastic constants.

From the presented approaches for setting up the numerical models, defining the boundary and loading conditions and carrying out the evaluation of strains, it was demonstrated that the analytical results can be satisfactorily reproduced. A clear effect of interface friction on the resulting axial stress distributions was detected, with the highest influence given for samples with an isotropy plane inclination of $\beta = 45°$. The resulting strains at the central cross section showed almost no dependency on the considered interface friction, except for the radial strains of the samples with $\beta = 45°$. By evaluating the results of 15 numerical UCS test simulations on moderately anisotropic rock samples, i.e., $E/E' \sim 2$, with friction considered at the sample–platen contacts and varying values for the transverse shear modulus G' and ratio ν/ν', it was found that both variation parameters affect the resulting strains in the x-direction for samples with inclined planes. High values for G' in combination with low ratios ν/ν' resulted in the maximum difference between analytical and numerical values for the strain component ϵ_x of ~15%. Despite this high discrepancy, the value of the back-calibrated transverse shear modulus G' only diverged by ~3% from the value as used for the simulation. This range is considered too small to justify

the requirement of friction-reducing measures, e.g., ball-bearing plates, within UCS tests on moderately anisotropic rocks. Considering that, in physical UCS tests, plasticity and complex micro-mechanical processes are also contributing to the developing sample strains, specimen end-effects might not be the biggest contributing factor toward inaccuracies in calibration results provided that the strain measurements are carried out locally.

The findings of the present research on the elastic behavior of transversely isotropic cylindrical rock specimens under uniaxial compression can be summarized as follows:

- The majority of transversely isotropic rocks possess elastic parameters that fall within observable standard domains.
- A polar representation of analytical strain distributions confronted with actual measurement values can help in identifying bad measurement results.
- Slight deviations from the optimum strain measurement directions may result in large errors in the measurements given that strain gradients are highest in close proximity to these directions.
- Provided that local strain measurements are carried out, a practically relevant influence of end-effects is only to be expected for generated radial strains around samples with inclined isotropy planes.
- End-effects are found to be associated only with influences on the transverse shear modulus G' when employing the standard procedure for the calibration of the elastic constants in terms of secant values. However, a maximum deviation of the back-calibrated values for G' of only $\sim$3% from the used values in the numerical simulations was detected, associated with the case of the highest adopted value for G' and the lowest ratio ν/ν'. This small discrepancy existed despite a larger observed difference of $\sim$15% between the analytical (without end-effects) and numerical (with end-effects) results for the strain measure ε_x in the dip direction of samples with inclined isotropy planes evaluated at a stress level of 10 MPa. Strain measure ε_x represents the strain measure as used for the back-calibration of G'.
- For the numerical investigation of UCS test end-effects on the deformation behavior of anisotropic rocks with a pronounced non-linear and plastic behavior, the adoption of a linear elastic transversely isotropic material model, as considered in this study, will be a limiting factor. In such cases, the utilization of more sophisticated material models, capable of representing the mentioned material peculiarities, will be required.

Our theoretical study suggests that frictional end-effects at the sample–platen contact within UCS tests on transversely isotropic specimens with a predominantly linear behavior and low to moderate degrees of anisotropy do not substantially influence the calibration results for the elastic parameters, in case strains are measured using local measuring arrangements. From this point of view, the necessity of special friction-reducing measures is not given. Validating laboratory experiments supporting this statement are currently under preparation.

References

1. Barton, N.; Quadros, E. Anisotropy is Everywhere, to See, to Measure, and to Model. *Rock Mech. Rock Eng.* **2015**, *48*, 1323–1339. [CrossRef]
2. Amadei, B. Importance of anisotropy when estimating and measuring in situ stresses in rock. *Int. J. Rock Mech. Min. Sci. Geomech. Abstr.* **1996**, *33*, 293–325. [CrossRef]
3. Pietruszczak, S.; Lydzba, D.; Shao, J. Modelling of inherent anisotropy in sedimentary rocks. *Int. J. Solids Struct.* **2002**, *39*, 637–648. [CrossRef]
4. Kwaśniewski, M.A. Mechanical Behavior of Anisotropic Rocks. In *Comprehensive Rock Engineering*; Hudson, J.A., Ed.; Pergamon Press: Oxford, UK, 1993; Volume 1, pp. 285–312.
5. Amadei, B.; Savage, W.Z.; Swolfs, H.S. Gravitational stresses in anisotropic rock masses. *Int. J. Rock Mech. Min. Sci. Geomech. Abstr.* **1987**, *24*, 5–14. [CrossRef]
6. Asaka, M.; Holt, R.M. Anisotropic Wellbore Stability Analysis: Impact on Failure Prediction. *Rock Mech. Rock Eng.* **2021**, *54*, 583–605. [CrossRef]
7. Amadei, B. In situ stress measurements in anisotropic rock. *Int. J. Rock Mech. Min. Sci. Geomech. Abstr.* **1984**, *21*, 327–338. [CrossRef]
8. Hakala, M.; Kuula, H.; Hudson, J.A. Estimating the transversely isotropic elastic intact rock properties for in situ stress measurement data reduction: A case study of the Olkiluoto mica gneiss, Finland. *Int. J. Rock Mech. Min. Sci.* **2007**, *44*, 14–46. [CrossRef]
9. Liu, L.; Chalaturnyk, R.; Deisman, N.; Zambrano-Narvaez, G. Anisotropic borehole response from pressuremeter testing in deep clay shale formations. *Can. Geotech. J.* **2021**, *58*, 1159–1179. [CrossRef]
10. Barla, G. Rock Anisotropy: Theory and Laboratory Testing. In *Rock Mechanics*; Müller, L., Ed.; Springer: Vienna, Austria, 1972; pp. 131–169. [CrossRef]
11. Lekhnitskii, S.G. *Theory of Elasticity of an Anisotropic Body*; MIR Publishers: Moscow, Russia, 1981.
12. Shen, L.W.; Playter, T. Determining the transverse isotropic rocks' static elastic moduli with cylindrical plugs: Shortfalls, challenges, and expected outcomes. *Geophysics* **2021**, *86*, W31–W46. [CrossRef]
13. Cho, J.W.; Kim, H.; Jeon, S.; Min, K.B. Deformation and strength anisotropy of Asan gneiss, Boryeong shale, and Yeoncheon schist. *Int. J. Rock Mech. Min. Sci.* **2012**, *50*, 158–169. [CrossRef]
14. Alejano, L.R.; González-Fernández, M.A.; Estévez-Ventosa, X.; Song, F.; Delgado-Martín, J.; Muñoz-Ibáñez, A.; González-Molano, N.; Alvarellos, J. Anisotropic deformability and strength of slate from NW-Spain. *Int. J. Rock Mech. Min. Sci.* **2021**, *148*, 104923. [CrossRef]
15. Winkler, M.B.; Frühwirt, T.; Marcher, T. A theoretical framework for calibrating the transversely isotropic elastic rock parameters from UCS tests on cylindrical specimens using circumferential strain measurements. In Proceedings of the 15th International Congress on Rock Mechanics and Rock Engineering & 72nd Geomechanics Colloquium—Challenges in Rock Mechanics and Rock Engineering, Salzburg, Austria, 9–14 October 2023; Schubert, W., Kluckner, A., Eds.; Austrian Society for Geomechanics: Salzburg, Austria, 2023; pp. 2478–2483.
16. Nejati, M.; Dambly, M.L.T.; Saar, M.O. A methodology to determine the elastic properties of anisotropic rocks from a single uniaxial compression test. *J. Rock Mech. Geotech. Eng.* **2019**, *11*, 1166–1183. [CrossRef]
17. Yim, J.; Lee, Y.; Hong, S.; Min, K.B. Determining Elastic Constants and Indirect Tensile Strength from a Single-Orientation Core of Transversely Isotropic Rock by the Uniaxial Compression and Brazilian Tests. In Proceedings of the 56th U.S. Rock Mechanics/Geomechanics Symposium, Santa Fe, NM, USA, 26–29 June 2022. [CrossRef]
18. Yim, J.; Hong, S.; Lee, Y.; Min, K.B. A novel method to determine five elastic constants of a transversely isotropic rock using a single-orientation core by strip load test and strain inversion. *Int. J. Rock Mech. Min. Sci.* **2022**, *154*, 105115. [CrossRef]
19. Lee, Y.; Yim, J.; Hong, S.; Min, K.B. Application of artificial neural network for determining elastic constants of a transversely isotropic rock from a single-orientation core. *Int. J. Rock Mech. Min. Sci.* **2022**, *160*, 105277. [CrossRef]
20. Alsuwaidi, E.S.; Xi, G.; Zimmerman, R.W. Mechanical characterization of Laffan and Nahr Umr anisotropic shales. *J. Pet. Sci. Eng.* **2021**, *200*, 108195. [CrossRef]
21. Li, K.; Yin, Z.Y.; Han, D.; Fan, X.; Cao, R.; Lin, H. Size Effect and Anisotropy in a Transversely Isotropic Rock Under Compressive Conditions. *Rock Mech. Rock Eng.* **2021**, *54*, 4639–4662. [CrossRef]
22. Song, F.; González-Fernández, M.A.; Rodriguez-Dono, A.; Alejano, L.R. Numerical analysis of anisotropic stiffness and strength for geomaterials. *J. Rock Mech. Geotech. Eng.* **2022**, *15*, 323–338. [CrossRef]
23. Perbawa, A.; Gramajo, E.; Finkbeiner, T.; Santamarina, J.C. Rock Triaxial Tests: Global Deformation vs. Local Strain Measurements—Implications. *Rock Mech. Rock Eng.* **2021**, *54*, 3527–3540. [CrossRef]
24. Togashi, Y.; Kikumoto, M.; Tani, K. An Experimental Method to Determine the Elastic Properties of Transversely Isotropic Rocks by a Single Triaxial Test. *Rock Mech. Rock Eng.* **2017**, *50*, 1–15. [CrossRef]
25. Dambly, M.L.T.; Nejati, M.; Vogler, D.; Saar, M.O. On the direct measurement of shear moduli in transversely isotropic rocks using the uniaxial compression test. *Int. J. Rock Mech. Min. Sci.* **2019**, *113*, 220–240. [CrossRef]
26. Gholami, R.; Rasouli, V. Mechanical and Elastic Properties of Transversely Isotropic Slate. *Rock Mech. Rock Eng.* **2014**, *47*, 1763–1773. [CrossRef]

27. Lama, R.D.; Vutukuri, V.S. *Handbook on Mechanical Properties of Rocks: Testing Techniques and Results: Volume II*; Series on Rock and Soil Mechanics; Trans Tech Publications: Aedermannsdorf, Switzerland, 1978.
28. Worotnicki, G. CSIRO Triaxial Stress Measurement Cell. In *Comprehensive Rock Engineering*; Hudson, J.A., Ed.; Pergamon Press Ltd: Oxford, UK, 1993; Volume 3, pp. 329–394. [CrossRef]
29. Batugin, S.A.; Nirenburg, R.K. Approximate relation between the elastic constants of anisotropic rocks and the anisotropy parameters. *Sov. Min. Sci.* **1972**, *8*, 5–9. [CrossRef]
30. Gerrard, C.M. Background to mathematical modelling in geomechanics: The role of fabric and stress history. In *Finite Elements in Geomechanics*; Gudehus, G., Ed.; Wiley: Chichester, UK, 1977; pp. 33–120.
31. Małkowski, P.; Ostrowski, Ł.; Brodny, J. Analysis of Young's modulus for Carboniferous sedimentary rocks and its relationship with uniaxial compressive strength using different methods of modulus determination. *J. Sustain. Min.* **2018**, *17*, 145–157. [CrossRef]
32. Sayers, C.M. The effect of anisotropy on the Young's moduli and Poisson's ratios of shales. *Geophys. Prospect.* **2013**, *61*, 416–426. [CrossRef]
33. Gercek, H. Poisson's ratio values for rocks. *Int. J. Rock Mech. Min. Sci.* **2007**, *44*, 1–13. [CrossRef]
34. Ji, S.; Li, L.; Motra, H.B.; Wuttke, F.; Sun, S.; Michibayashi, K.; Salisbury, M.H. Poisson's Ratio and Auxetic Properties of Natural Rocks. *J. Geophys. Res. Solid Earth* **2018**, *123*, 1161–1185. [CrossRef]
35. Graham, J.; Houlsby, G.T. Anisotropic elasticity of a natural clay. *Géotechnique* **1983**, *33*, 165–180. [CrossRef]
36. Jin, Z.; Li, W.; Jin, C.; Hambleton, J.; Cusatis, G. Elastic, strength, and fracture properties of Marcellus shale. *Int. J. Rock Mech. Min. Sci.* **2018**, *109*, 124–137. [CrossRef]
37. Saint-Venant, B. Sur la distribution des élasticités autour de chaque point d'un solide ou d'un milieu de contexture quelconque, particulièrement lorsqu'il est amorphe sans être isotrope. *J. Math. Pures Appl. Ser.* **1863**, *8*, 257–430.
38. Talesnick, M.L.; Ringel, M. Completing the hollow cylinder methodology for testing of transversely isotropic rocks: Torsion testing. *Int. J. Rock Mech. Min. Sci.* **1999**, *36*, 627–639. [CrossRef]
39. Wittke, W. *Rock Mechanics Based on an Anisotropic Jointed Rock Model (AJRM)*, 1st ed.; Wilhelm Ernst & Sohn Verlag fur Architektur und Technische: Berlin, Germany, 2014. [CrossRef]
40. PLAXIS Reference Manual: 3D—Connect Edition V21. 2021. Available online: https://communities.bentley.com/cfs-file/__key/communityserver-wikis-components-files/00-00-00-05-58/PLAXIS3DCE_2D00_V21.01_2D00_02_2D00_Reference.pdf (accessed on 20 September 2023)
41. Mutschler, T. Neufassung der Empfehlung Nr. 1 des Arbeitskreises "Versuchstechnik Fels" der Deutschen Gesellschaft für Geotechnik e. V.: Einaxiale Druckversuche an zylindrischen Gesteinsprüfkörpern. *Bautechnik* **2004**, *81*, 825–834. [CrossRef]
42. Rukavishnikov, V.A.; Rukavishnikova, E.I. Comparative analysis of the finite element methods for the elasticity problem with singularity. In Proceedings of the International Conference of Numerical Analysis and Applied Mathematics (ICNAAM), Rhodes, Greece, 13–18 September 2018; AIP Publishing: Melville, NY, USA, 2019; AIP Conference Proceedings 2116; p. 450042. [CrossRef]
43. Wei, X.X.; Chau, K.T. Finite and transversely isotropic elastic cylinders under compression with end constraint induced by friction. *Int. J. Solids Struct.* **2009**, *46*, 1953–1965. [CrossRef]